Astronomy & Astrophysics manuscript no. sdbchannel
May 10, 2008

A seismic approach to test different formation channels of subdwarf B stars

Haili Hu[1,2], M.-A. Dupret[3], C. Aerts[1,2], G. Nelemans[1], S. D. Kawaler[4], A. Miglio[5], J. Montalban[5], and R. Scuflaire[5]

[1] Department of Astrophysics, IMAPP, Radboud University Nijmegen, PO Box 9010, 6500 GL, Nijmegen, the Netherlands
e-mail: hailihu@astro.ru.nl
[2] Institute of Astronomy, Katholieke Universiteit Leuven, Celestijnenlaan 200D, 3001 Leuven, Belgium
[3] Observatoire de Paris, LESIA, 5 place Jules Janssen, 92195 Meudon Principal Cedex, France
[4] Department of Physics and Astronomy, Iowah State Univeristy, Ames, IA 50014, USA
[5] Institute d'Astrophysique et Géophysique, université de Liège, Belgium

;

ABSTRACT

Context. There are many unknowns surrounding the formation of subdwarf B stars, and different formation channels are considered to be possible. Nevertheless, seismic models up to date assume that an sdB star is a post-helium-flash-core surrounded by a thin inert layer of hydrogen.
Aims. We examine an alternative formation channel, in which the sdB star originates from a massive ($> \sim 2$ M$_\odot$) Red Giant with a non-degenerate He-core. Although these sdB stars may evolve through the same region of the $\log g - T_{\rm eff}$ diagram as the canonical post-flash sdB stars, their interior structure is rather different. We are interested in how this affects their pulsation modes and whether this can be observed.
Methods. Using detailed stellar evolution calculations we construct sdB models from both formation channels. The iron enhancement in the driving region due to diffusion, which causes the excitation of the modes, is approximated by a Gaussian increase. The pulsation modes and frequencies are calculated with a non-adiabatic pulsation code.
Results. A detailed comparison of two sdB models from different channels, but with same $\log g$ and $T_{\rm eff}$, shows that the mode excitation is significantly different. The excited frequencies are smaller for the post-flash sdB star than for the post-non-degenerate sdB star. This is a direct result of the differing chemical compositions in the envelope. A more general comparison between two grids of models, tells us that for most post-non-degenerate sdB stars, their excited frequencies cannot be well-matched with the frequencies, excited or non-excited, of a post-flash sdB star. In the rare event that an acceptable seismic match is found, additional information, such as mode identification and $\log g$ and $T_{\rm eff}$ determinations, allows us to discriminate between the two formation channels.

Key words. subdwarfs – stars: evolution – stars: oscillation – methods: numerical

1. Introduction

Commonly, subdwarf B (sdB) stars are identified as Extreme Horizontal Branch (EHB) stars, and they are believed to be post-He-core-flash products with core masses around $\sim$0.5 M$_\odot$ surrounded by a very thin inert hydrogen-envelope (Heber 1986; Saffer et al. 1994). From a single stellar evolution point of view this can be explained by enhanced mass loss of stars close to helium ignition with very lightly bound envelopes (D'Cruz et al. 1996), i.e. stars with degenerate cores near the tip of the Red Giant Branch (RGB). However, as they are frequently observed in binaries (e.g. Allard et al. 1994; Morales-Rueda et al. 2006), binary interactions most likely play an important role in their formation. Han et al. (2002) explored the main binary evolution channels that can produce sdB stars: common-envelope ejection (CEE), stable Roche lobe overflow (RLOF) and helium white dwarf (WD) mergers. They found that the sdB mass distribution may be much broader than previously thought, 0.3 – 0.8 M$_\odot$ instead of 0.4 – 0.5 M$_\odot$. The sdB stars with non-canonical masses follow from WD mergers or massive ($> \sim 2$ M$_\odot$) progenitors that ignite helium quiescently, where the latter can be a subchannel of either the CEE channel or the stable RLOF channel. Binary population synthesis show that the more massive progenitors do not contribute significantly to the sdB population (Han et al. 2003). But one should keep in mind that in such BPS studies it is asumed that CE evolution is described by the α formalism, i.e. that the CE ejection is driven by the orbital energy. As the physics of the CE phase is poorly understood, other scenarios cannot be excluded a priori. For example, the γ-formalism proposed by Nelemans et al. (2000), based on the angular momentum equation rather than the energy equation, provides an alternative description. In this case, the massive Red Giants cannot be ruled out as possible sdB progenitors (Hu et al. 2007). We therefore want to explore the possibility of this neglected class of progenitors in a different manner, by using the seismic properties that have been observed in some sdB stars.

Although the post-He-flash and the post-non-degenerate sdB stars can appear in the same $\log g - T_{\rm eff}$ region, their interior structures are quite different. In particular, the chemical composition profiles differ greatly depending on whether the sdB star ignited in a flash or quiescently. The canonical post-He flash sdB star has a very narrow He−H transition zone, while the sdB star created from a more massive progentior has a much broader H-profile. This is a direct result of the differing chemical compositions between low mass and high mass stars on the RGB owing

Send offprint requests to: H. Hu

to the different convective regions during the MS and RGB evolution. We examine, in this paper, whether these differences in the interior structure will result in observable differences in the pulsation modes.

The sdB pulsators consist of two classes, the short-period variable EC 14026 stars (Kilkenny et al. 1997), and the long-period variable PG 1716 stars (Green et al. 2003). The rapid oscillations in EC 14026 stars are interpreted in terms of low-order p-modes (Charpinet et al. 1996), driven by the κ-mechanism operating in the iron opacity bump (IOB). The same mechanism has been shown to excite long-period, high order g-modes in the cooler models (Fontaine et al. 2003). The local iron enhancement necessary in the driving region around $\log T \approx 5.3$ is due to the competing diffusion processes radiative levitation and gravitational settling. It is well-known that the opacities play an important role in the study of the pulsations. Seaton & Badnell (2004) showed that the IOB is situated at slightly higher temperatures using OP opacities (Seaton et al. 1994; Badnell & Seaton 2003) compared with OPAL opacities (Iglesias & Rogers 1996). Jeffery & Saio (2006) found that using OP opacities, and nickel enhancement in addition to that of iron, the theoretical instability strip of g-mode sdB oscillators is more consistent with observations. For our purposes it is sufficient to implement OPAL opacities and iron enhancement, since we are interested in the relative differences of two classes of sdB stars. We acknowledge the importance of including the effect of OP opacities and nickel enhancement in further detailed studies.

The details of the computations are given in section 2. The results are presented in Section 3. In Section 3.3, we compare the detailed physical characteristics of two reference models with different formation history. In Section 3.4 we compare the frequency characterics globally between two grids of models. The results and conclusions are discussed in Section 4.

2. Computations

2.1. The evolution calculations

We construct sdB structure models with the stellar evolution code developed by Eggleton (1971, 1972, 1973); Eggleton et al. (1973) and updated by Han et al. (1994) and Pols et al. (1995, 1998)[1]. The updated version of the code uses an equation of state that includes pressure ionization and Coulomb interaction, nuclear reaction rates from Caughlan et al. (1985) and Caughlan & Fowler (1988), and neutrino loss rates from Itoh et al. (1989, 1992). Both convective and semi-convective mixing are treated as diffusion processes. We use a mixing-length parameter (the ratio of the mixing-length to the local pressure scaleheight) of $\alpha = l/H_p = 2.0$. It is assumed that mixing occurs in the region where

$$\nabla_{\rm rad} > \nabla_{\rm ad} - \delta_{\rm ov}/(2.5 + 20\beta + 16\beta^2). \quad (1)$$

where β is the ratio of radiation pressure to gas pressure and $\delta_{\rm ov}$ is the overshooting parameter. Schroder et al. (1997) showed that $\delta_{\rm ov} = 0.12$ gives the best fit to observations of ζ Aurigae binaries, which corresponds to an overshooting length of $\sim 0.25 H_p$. For our comparative study it suffices to adopt $\delta_{\rm ov} = 0.12$, but keep in mind that core overshooting can in fact also be probed by asteroseismology, e.g. Aerts et al. (2003).

The metallicity is taken to be $Z = 0.02$, and the initial hydrogen and helium abundances follow as $X = 0.76 - 3.0Z$ and $Y = 0.24 + 2.0Z$. If it is not mentioned otherwise, the opacity tables are constructed by combining the OPAL opacities (Iglesias & Rogers 1996) with the conductive opacities (Hubbard & Lampe 1969; Canuto 1970; Iben 1975), as implemented in the Eggleton code by Eldridge & Tout (2004).

We start by evolving ZAMS models in the range $1 - 3$ M$_\odot$ to the tip of the RGB, adopting a Reimer's mass loss rate (Reimers 1975),

$$\dot{M}_{\rm wind} = 4 \times 10^{-13} \eta \frac{(R/R_\odot)(L/L_\odot)}{(M/M_\odot)} \ [{\rm M_\odot yr^{-1}}], \quad (2)$$

with an efficiency of $\eta = 0.4$ (Iben & Renzini 1983; Carraro et al. 1996). For simplicity, we do not include mass-loss on the EHB. Unglaub & Bues (2001) showed that, if the observed chemical abundances are a result of the combined effects of diffusion and mass loss, the EHB mass-loss rate should be in the range $10^{-14} \leq \dot{M}({\rm M_\odot yr^{-1}}) \leq 10^{-12}$. This is consistent with the rates found by Vink & Cassisi (2002) for radiation driven wind models. They also showed that these rates are too low to have a direct effect on the EHB evolution.

At the RGB tip we remove the envelope, while keeping the chemical compositions fixed. Thus, we assume that the mass transfer happens on a timescale much shorter than the nuclear timescale. This is a reasonable assumption for sdB stars in short-period binaries formed by CE ejection, which is the majority of the observed sdB stars (Maxted et al. 2001), and the focus of our study here. In the case that the He-flash occurs, Zero Age Horizontal Branch (ZAHB) models are artificialy created from a 2.25 M$_\odot$ He-core-burning star, where we reset the chemical positions to the values before the flash. For a more rigorous treatment, investigation of how the He-flash affects the chemical compositions is required.

During the EHB phase, we use for temperatures $\log T > 7$, the same opacities as mentioned above. In the outer layers of the star, $\log T < 7$, where the pulsation driving region is located, the opacities are calculated by interpolating between several OPAL tables computed with iron abundance enhanced by factors of $f =$ 1, 2, 5 , and 10 relative to solar, thus $X(Fe) = 0.071794Zf$. The abundances of the other heavy elements are decreased such that the overall metallicity is kept constant as in Miglio et al. (2007).

2.2. The oscillation calculations and iron accumulation

We adapted the Eggleton evolution code such that the output is suitable for pulsation calculations. In practice, this implied calculating some additional physical quantities during the evolution, and modifying the mesh to have sufficient meshpoints in the stellar envelope. The seismic properties of the stellar models are then calculated with two pulsation codes. The adiabatic code OSC by Scuflaire et al. (2007) is used to obtain the approximate frequencies which are used as a first guess in the linear non-adiabatic code MAD by Dupret (2001). We determine the theoretical frequency spectrum up to $l = 2$, since it is expected that higher order modes are geometrically canceled. Charpinet et al. (1996) established that the excitation of sdB oscillatons is related to a local enrichment of iron in the stellar envelope caused by diffusion. Radiative levitation is expected to set up significant chemical gradients within a diffusion timescale of $\sim 10^5$ yr and consequently iron accumulates around $\log T \approx 5.3$ (Michaud et al. 1989; Chayer et al. 1995). Time-dependent diffussion calculations (Fontaine et al. 2006) show that after $\sim 10^5$ yr many pulsation modes are excited. Since element diffusion is not treated in the evolution code, we use an approximation for

[1] A write-up of the most recent version of this code can be obtained from P. P. Eggleton at ppe@igpp.ucllnl.org.

the iron accumulation, where we assume that the iron only affects the stellar structure though the opacity. At each timestep of the evolution calculations the iron enhancement factor f is increased with a Gaussian centered at $\log T = 5.3$,

$$\frac{df}{dt} = \frac{(1 - f/10)^3}{\tau} \exp\Big(- \frac{(\log T - 5.3)^2}{\sigma^2}\Big), \quad (3)$$

with the initial condition $f(t = 0) = 1$. The width $\sigma^2 = 0.05$ and accumulation timescale $\tau = 4 \times 10^5$ yr are chosen such that iron is only increased in the region $4.5 < \log T < 6.1$, and $\lim_{t\to\infty} f = 10$, which is loosely based on the time-dependent diffusion calculations of Fontaine et al. (2006) and the equilibrium profiles of Charpinet et al. (1997). Our parametric approximation is rather ad hoc, but since we are interested in the relative differences between two different scenarios, the exact shape of the iron profile is not crucial here.

In Fig. 2, we show f throughout the star for different ages of an sdB star. Note that the temperature range $4.5 < \log T < 6.1$ corresponds to a very narrow mass shell of $\sim 10^{-6}$ $M_\odot$. In Fig. 2c, we included during the evolution the backreaction of convective mixing on our parametric iron profile. Notice that the iron abuncance is homogeneous near $\log T = 5.3$ ($\log q = -10$) and $\log T = 4.6$ ($\log q = -12.5$). This is caused by two narrow convective layers due to iron and helium ionization, respectively. Interestingly, we found that the convective region around $\log T = 5.3$ would not be present without iron accumulation. We determined that the slightly perturbed iron profile has negligible effect on the driving and the pulsation frequencies. Moreover, since our iron accumulation is of approximative nature, we have not included this effect in further calculations.

Table 1. The models in grid *A* and *B*. The label of the track given in the first column is used for reference in Fig. 6. The second column gives the number of seismic models along that tracks. The final column shows the mass of the ZAMS models from which the sdB star is created.

track	# models	$M_{\rm sdB}$ ($M_\odot$)	$M_{\rm env,0}$ ($M_\odot$)	$M_{\rm ZAMS}$ ($M_\odot$)
*A*1	27	0.42	0.0001	1.85
*A*2	27	0.42	0.0003	1.85
*A*3	27	0.42	0.0006	1.85
*A*4	25	0.43	0.0001	1.80
*A*5	25	0.43	0.0003	1.80
*A*6	25	0.43	0.0006	1.80
*A*7	23	0.44	0.0001	1.75
*A*8	23	0.44	0.0003	1.75
*A*9	23	0.44	0.0006	1.75
*A*10	21	0.45	0.0001	1.65
*A*11	21	0.45	0.0003	1.65
*A*12	21	0.45	0.0006	1.65
*A*13	20	0.46	0.0001	1.55
*A*14	20	0.46	0.0003	1.55
*A*15	20	0.46	0.0006	1.55
*A*16	18	0.47	0.0001	1.00
*A*17	18	0.47	0.0003	1.00
*A*18	18	0.47	0.0006	1.00
*B*1	23	0.44	0.005	2.75
*B*2	18	0.45	0.0075	2.75
*B*3	21	0.46	0.005	2.90
*B*4	18	0.47	0.0075	2.90
*B*5	18	0.47	0.005	3.00

3. Results

3.1. The stellar models

Following the procedure as described above, we construct a grid of canonical, i.e. post-He-flash, sdB models (hereafter called grid *A*) with masses in the range 0.42 – 0.47 $M_\odot$ in steps of 0.01 $M_\odot$. The maximum mass we obtain for the degenerate core of an RGB star is 0.47 $M_\odot$, thus we do not consider post-flash sdB stars above this mass. The H-envelope masses, $M_{\rm env,0}$, considered are 0.0001, 0.0003, and 0.0006 $M_\odot$, where $M_{\rm env,0}$ is defined as the total mass of the hydrogen content directly after the removal of the envelope. Thus, we have 18 sdB evolution tracks, which we follow until the end of He-core burning. After each 10^7 yr of EHB evolution, the seismic properties are calculated, and we only consider models with unstable modes. Since we do not find unstable modes in our post-He-core burning models, our analysis is limited to sdB stars in their He-core burning pahse. This leads to a total of 402 seismic models in the range of $T_{\rm eff} = 25,000 - 34,000$ K and $\log g = 5.4 - 6.0$.

The grid of non-canonical sdB stars (hereafter called grid *B*) consists of 5 tracks: ($M_{\rm sdB}$ ($M_\odot$), $M_{\rm env,0}$ ($M_\odot$)) = (0.44, 0.005), (0.45, 0.005), (0.46, 0.005), (0.47, 0.0075), and (0.47, 0.005). Along these tracks we have in total 98 seismic models, again taken after each 10^7 yr of EHB evolution. In Table 1, more details about the models are given.

The EHB evolution tracks and the seismic models can be seen in Fig. 1. The tracks start directly after the removal of the envelope. For the post-flash models this corresponds to the ZAEHB. The post-non-degenerate models have hydrogen extending to deeper layers, hence allowing some H-shell-burning, before reaching the ZAEHB. Notice that although the two different classes of sdB star can evolve through the same $\log g - T_{\rm eff}$ during core-He-burning, the post-He-core-burning evolution differs. The post-non-degenerate sdB star has again a short phase ($\sim 10^6$ yr) of H-shell burning, before starting He-shell-burning, see Fig. 1b.

3.2. Effects of the iron accumulation

In Fig. 3, we show the effect of different iron abundance profiles on the EHB evolution in a $\log g - T_{\rm eff}$ diagram. We compare our parametric approach to no iron enhancement ($f = 1$), and a uniform enhancement of $f = 10$ in the whole envelope, as has been used in studies of mode excitation (Jeffery & Saio 2006). It is evident that using $f = 10$ influences the evolution drastically, while the Gaussian increase has little effect. This is because higher iron abundances give higher opacities, and thus larger stellar radii. With our approximated profile we only increase iron in a relatively small region, resulting in a minimal effect on the stellar structure. However, a minimal change of the stellar structure can result in a visible shift of the pulsation frequencies, as has been shown by Fontaine et al. (2006).

We also compare the effect on the excitation, and find that our approximated iron profile can excite almost as many modes as the $f = 10$ enhancement, see Fig. 4a-c. This is because the driving mechanism in sdB stars is associated with the iron opacity bump, and accumulating iron in this driving region is sufficient for the excitation of the pulsation modes, see Fig. 4d-f. Thus, with our parametric approach to iron accumulation the issue of excitation can be addressed, while keeping the effect of the iron profile on the stellar structure to a more realistic minimum. Furthermore, these are the first evolutionary models of sdB stars that include the effect of iron accumulation, albeit in an approximative manner.

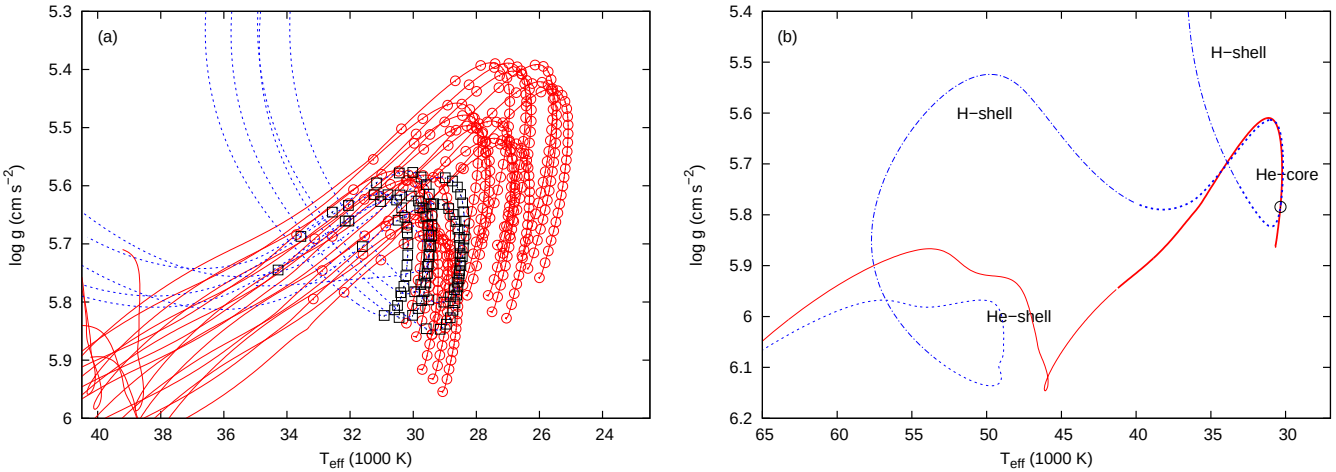

Fig. 1. (a) EHB Evolutionary tracks in the ł$ogg - T_{\rm eff}$ diagram. The solid curves correspond to the post-flash sdB models, and the dotted curves to the post-non-degenerate sdB models. The circles and squares indicate models on which we performed pulsation calculations for the post-flash and post-non-degenerate tracks respectively. (b) Evolutionary tracks of a post-flash sdB star created from of low-mass ($M_{\rm zams}$ = 1.00 $M_\odot$), and a post-non-degenerate sdB star created from a high mass ($M_{\rm zams}$ = 3.00 $M_\odot$) progenitor, given by the solid and dotted curve respectively. Along the tracks the dominant energy source (either H-shell-burning, He-core-burning or He-shell-burning) is noted. The bold part of the tracks indicate the He-core-burning phase and the thin part the He-shell burning phase. During the dot-dashed parts of the post-non-degenerate track, H-shell burning is the dominant energy source. At the circle in (b), we selected from both tracks a model for a detailed comparison, see Section 3.3.

3.3. Comparing two representative models

We examine the physical differences in the interior structure of a post-flash (α) and a post-degenerate (β) sdB with same $\log g$ and $T_{\rm eff}$. We choose as representative models the ones circled in Fig. 1b at $\log g = 5.78$ and $T_{\rm eff} = 30$ kK. One of the main differences is the abundance profiles, see Fig. 5a. The He-H transition layer of β is much broader and located deeper in the star. The envelope of β is in the region where the shrinking convective core passed through during the MS, hence the low H-abundance here: $X = 0.18$. For α, the helium core has grown into the region that used to be part of the convective envelope during the RGB, and as a result the He-H transition region is much narrower and the H-abundance in the envelope is around $X = 0.66$. In Fig. 5d, we show the iron mass fractions, and in Fig. 5e the resulting opacity profiles. The outer opacity bump near $\log T = 4.7$ is associated with He-ionization, the iron opacity bump near $\log T = 5.3$ is heightened by the local iron accumulation.

Two important quantites in stellar pulsation theory are the the Brunt-Väisäla frequency N and the Lamb frequencies L_l,

$$N^2 = \frac{Gm}{r^2}\frac{\delta}{H_p}\left(\nabla_{\rm ad} - \nabla + \frac{\varphi}{\delta}\nabla_\mu\right) \tag{4}$$

$$\text{with} \quad \delta = -\frac{\partial \ln \rho}{\partial \ln T} \quad \text{and} \quad \varphi = \frac{\partial \ln \rho}{\partial \ln \mu}$$

$$L_l^2 = \frac{l(l+1)c_s^2}{r^2}, \tag{5}$$

where μ is the molecular weight and c_s^2 is the adiabatic sound speed. Notice that when $N^2 < 0$, the Ledoux criterion for dynamical stability is violated (Ledoux 1947). Thus, in Fig. 5b&c, the convective regions can be clearly identified. The most inner one is related to the convective core, and the outer two are the narrow convective layers due to iron (near $\log T = 5.3$) and helium ionization (near $\log T = 4.6$). Also, chemical gradients are apparent in N^2 in the form of localized peaks. The peak near the center is identified with the C-O/He transition zone and the more outer peak to the He-H transition zone. The Lamb frequencies are plotted in the same figure to indicate the propagation zones of the g-modes, $\sigma^2 < (N^2, L_l^2)$, and the p-modes, $\sigma^2 > (N^2, L_l^2)$, where σ is the angular pulsation frequency. It is apparent that g-modes are deep interior modes, while p-modes probe the superficial outer layers as pointed out by Charpinet et al. (2000).

Clearly, model α and β have quite different physical characteristics. To establish how this affects their seismic properties, we compare their frequencies in Fig. 5e. Since the large frequency separation $\Delta f = f_{n,l} - f_{n-1,l}$ is mainly dependent on the dynamical timescale, we see that Δf at high frequencies is more or less the same for the two models. The lower frequencies however, are in fact mixed modes which are more sensitive to the core, and we see a better distinction between model α and β here.

Moreover, the frequency ranges of excited $l = 0 - 2$ modes are not the same for these two models; for model α this range is [3.4 mHz, 10.6 mHz] and for model β it is [5.7 mHz,14.2 mHz]. In other words, the excited modes have smaller frequencies in model α than in model β. To understand this, we compare in Fig. 5h&i the work integral for these two models for the radial mode p_7. The work integral increases towards the surface in the driving region and decreases towards the surface in damping regions. The surface value is the dimensionless growth rate, positive for unstable modes and negative for stable ones. We see that p_7 is unstable in model β, but it is stable in model α, which is also indicated in Fig. 5i.

A first possible origin of the differences could come from the opacity, since the driving is a κ-mechanism operating in the iron opacity bump. Fig. 5b shows that the opacity is slightly larger for model β. The driving is thus a little more efficient in model β.

But this is not the main source of differences. Since the envelope H-fraction much smaller in model β ($X = 0.18$) than in model α ($X = 0.66$), the molecular weight is larger and, at given temperature, the density is significantly larger ($\sim$1.50$\times$) in model β, as shown by Fig. 5f. The driving of the modes is related to

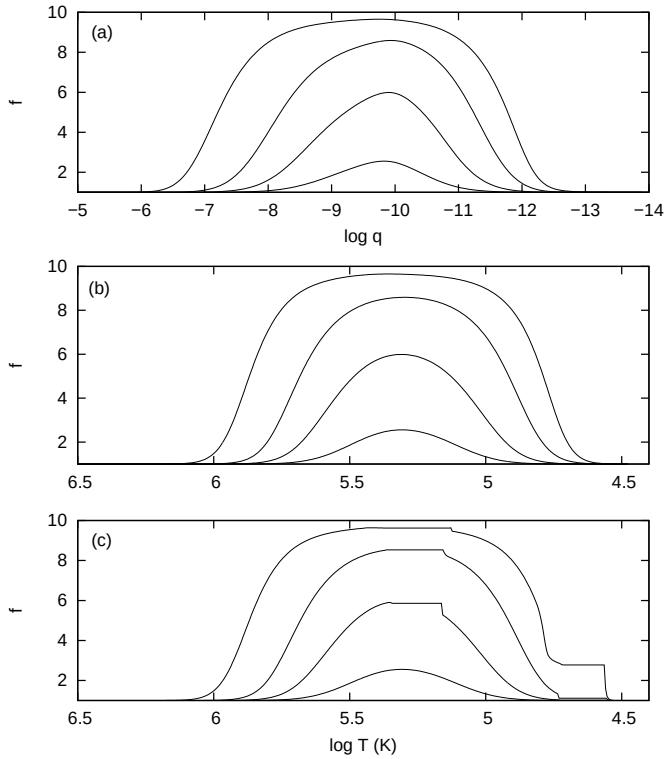

Fig. 2. The iron increase factor f throughout the star as a function of (a) the outer mass fraction: $\log q = \log\left(1 - \frac{M_r}{M_*}\right)$, and (b) the temperature. In panel (c) we show the effect of convective mixing on our parametric iron profile. The sdB star has $M_{\rm core} = 0.47$ M$_\odot$ and $M_{\rm env} = 10^{-4}$ M$_\odot$ at the ZAEHB, and was constructed from a 1.00 M$_\odot$ ZAMS model. The profiles from bottom to top correspond to sdB ages 10^5, 10^6, 10^7, 1.8×10^8 yr, where the last model is at the end of core-He-burning.

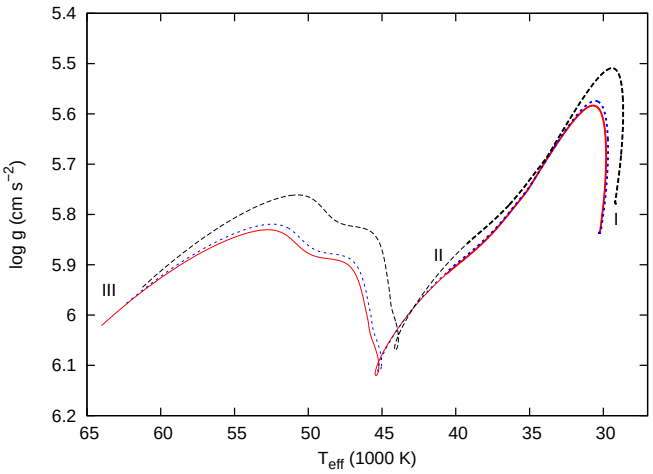

Fig. 3. Evolutionary tracks in the $\log g - T_{\rm eff}$ diagram of sdB stars with different iron profiles. The three tracks start at the same ZAHB model with $M_{\rm core} = 0.47$ M$_\odot$ and $M_{\rm env} = 10^{-4}$ M$_\odot$, created from a 1.00 M$_\odot$ ZAMS model. The lowest solid curve is for a model with no iron enhancement, the middle dotted curve is for a Gaussian iron increase centred at $\log T = 5.3$, and the upper dashed curve is for iron increased with a factor 10 uniformly in the envelope. The labels I, II, II, indicate the ZAHB, the end of core-He burning and the end of He-shell burning respectively. It takes the sdB star 1.8×10^8 yr to evolve from I to II, and 10^7 yr from II to III.

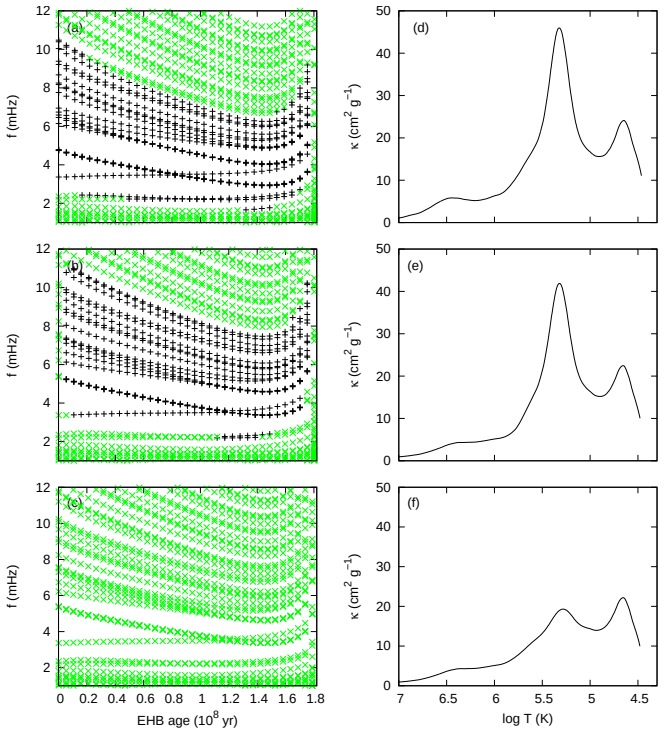

Fig. 4. Left: the frequencies of the stable (×) and unstable (+) modes ($l \leqq 2$) as a function of the EHB lifetime for the three tracks given in Fig. 3. Right: the opacity as a function of the temperature after 10^7 yr of EHB evolution. Panels (a&d) correspond to $f = 10$, (b&e) are for the Gaussian increase and (c&f) are for the model with no iron enhancement.

the opacity which is mainly a function of temperature. Hence, if the eigenfunctions of two given modes have the same shape as a function of temperature, the driving is the same. Here we compare the modes p_7 of two models with same radius, and as it is usually found for p-modes, their last node is located at the same geometrical distance from the surface Δr. But the gradient of temperature is not the same for the two models: $|\nabla T| \propto \kappa\rho$ is larger in model β because of the larger density. Hence the difference between the temperature at the last node and at the surface: $|\Delta T| \simeq |dT/dr|\,\Delta r$ is larger in model β than in model α. This is exactly what we find in Fig. 5i where the eigenfunction $|\delta T/T|$ is given: in terms of temperature, the last node is closer to the surface in model α compared to model β. To get the same driving as in model β, the last node of model α would have to be deeper in the star, which is only possible by considering a mode with smaller radial order and frequency. We understand thus why the frequencies of excited modes are smaller in model α than in model β.

3.4. Comparing two grids of models

Now we want to establish if it observationally possible to discriminate between a post-He-flash (a) and a post-non-degenerate sdB star (b). Imagine we observed the frequencies of b, is it then possible to find an acceptable seismic match in our grid of canonical post-flash models (grid A)? We take as 'observed'

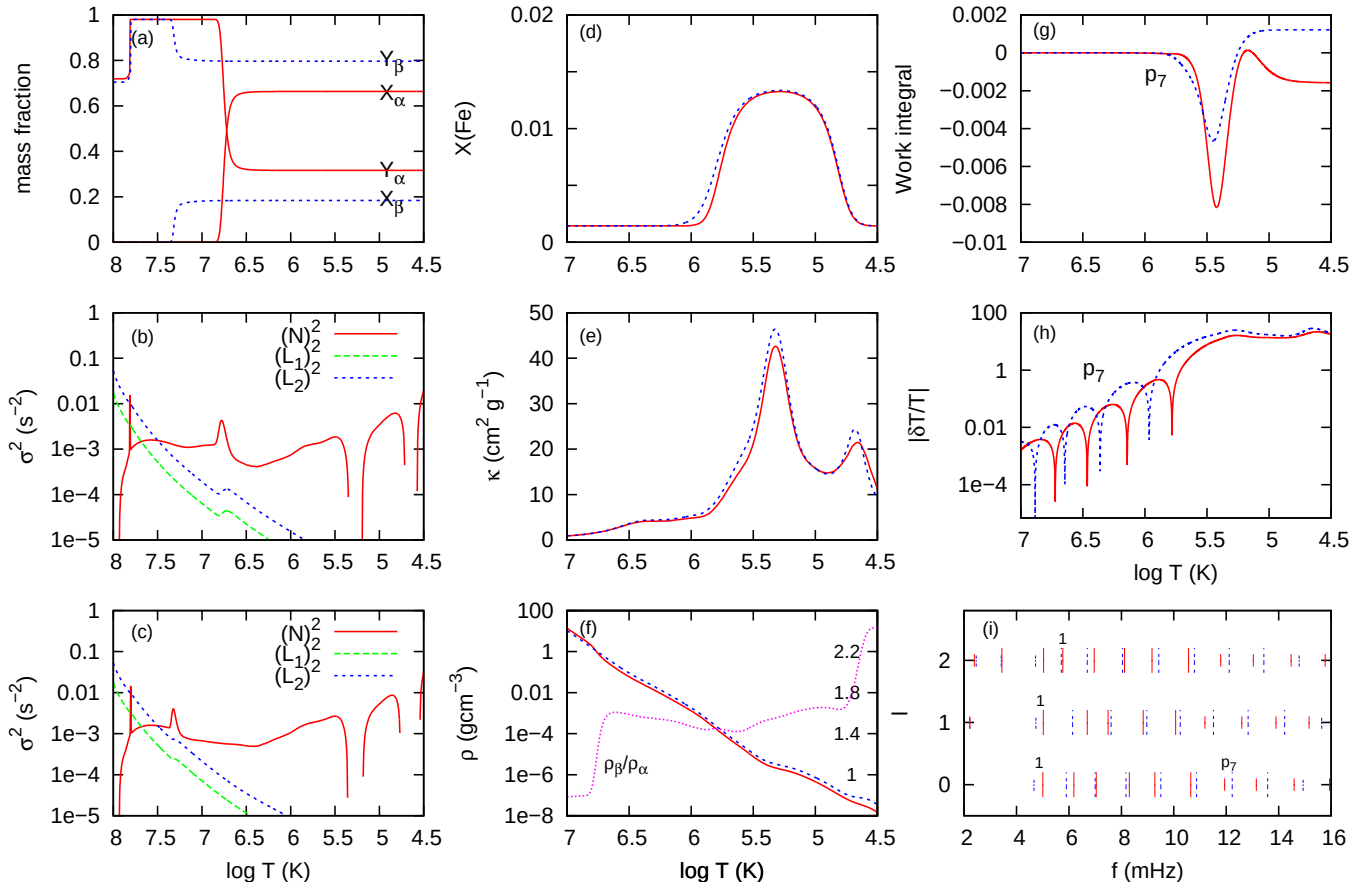

Fig. 5. Physical and seismic quantities of the two representative models α (post-flash) and β (post-non-degenerate). Panels (a)-(h) show various profiles as a function of the temperature: (a) the hydrogen (X) and helium (Y) mass fractions; (b)&(c) the Brunt-Vaisala and Lamb frequencies for model α and β respectively; (d) the iron mass fraction; (e) the opacity; (f) the density, we also plotted the density ratio ρ_β/ρ_α on the right axis; (g) the work integral for radial mode p_7; and (h) the eigenfunction $|\delta T/T|$ for the radial mode p_7. Panel (i) gives the pulsation frequencies for modes $l = 0 - 2$, where unstable modes are given by long line segments, and stable modes by short line segments. We indicated the modes with radial order 1, and radial mode p_7. In all panels, except (b)&(c), solid lines represent model α and dotted lines are for model β. Note that panels (a)-(c) give the profiles throughout the entire star, while the profiles in panels (d)-(h) are for the stellar envelope.

frequencies the frequencies of unstable modes up to $l = 2$. We do this for each model b in grid B, thus finding the best seismic match within the grids A and B.

Since for p-modes, the frequency separations follow from the asymptotic relations, we feel that frequency is the natural base for model comparison. To quantify 'acceptable', we use the merit function

$$\mathcal{M}^2 = \frac{1}{n_b}\sum_{i=1}^{n_b}(f_a^i - f_b^i)^2, \quad (6)$$

where f_b^i is one of the n_b excited frequencies of star b. The frequency matching is done such that $\mathcal{M}^2$ is minimized by brute force fitting. It is clear that the lower $\mathcal{M}^2$ is, the better the match between a and b is. Matches with $\mathcal{M}^2 > 0.05$ are considered insignificant, which is a generous limit, as we will see later. We investigate four different scenarios:

(i) We are not able to identify the modes, $\log g$ and $T_{\rm eff}$ of the 'observed' star b are unknown, and the 'observed' frequencies are allowed to be matched with both stable and unstable frequencies of the 'theoretical' model a.
(ii) Same as (i), except the modes are identified, thus the l-value must be matched.
(iii) Same as (i), except $\log g$ and $T_{\rm eff}$ are known within errors of $d\log g = 0.1$ and $dT_{\rm eff} = 1000K$.
(iv) Same as (i), except the 'observed' frequencies are only matched with unstable 'theoretical' frequencies.

In Fig. 6 we show $\mathcal{M}^2$ for each gridpoint in grids A and B for the scenarios (i)-(iv). The matches with low $\mathcal{M}^2$ are visible as dark diagonally regions, This is a result of the change in frequencies during the EHB evolution.

The matches with lowest $\mathcal{M}^2$ are circeled in Fig. 6 and details of these models are shown in Fig, 7 and Table 3.4. We remark that for all scenarios the best matches are found for the same model b, namely the last model of evolutionary track $B5$. This is because in this model only the higher frequencies are excited. As we discussed in section 3.3, the lower frequencies are more sensitive to the deeper layers, thus the distinction between models a and b is better detected at low frequencies.

As comparison we refer Brassard et al. (2001), their optimal model for PG 0014+067 has a $\chi^2 = 0.5374$, where χ^2 is a merit function based on period comparison. Translated to our frequency merit function this is equivalent to $\mathcal{M}^2 = 0.0084$. We find, in principle, seismic matches between a and b with $\mathcal{M}^2$ of this order for scenarios (i)-(iii). However, it is visible in Fig. 6 that the number of matches with $\mathcal{M}^2$ of this order is quite small

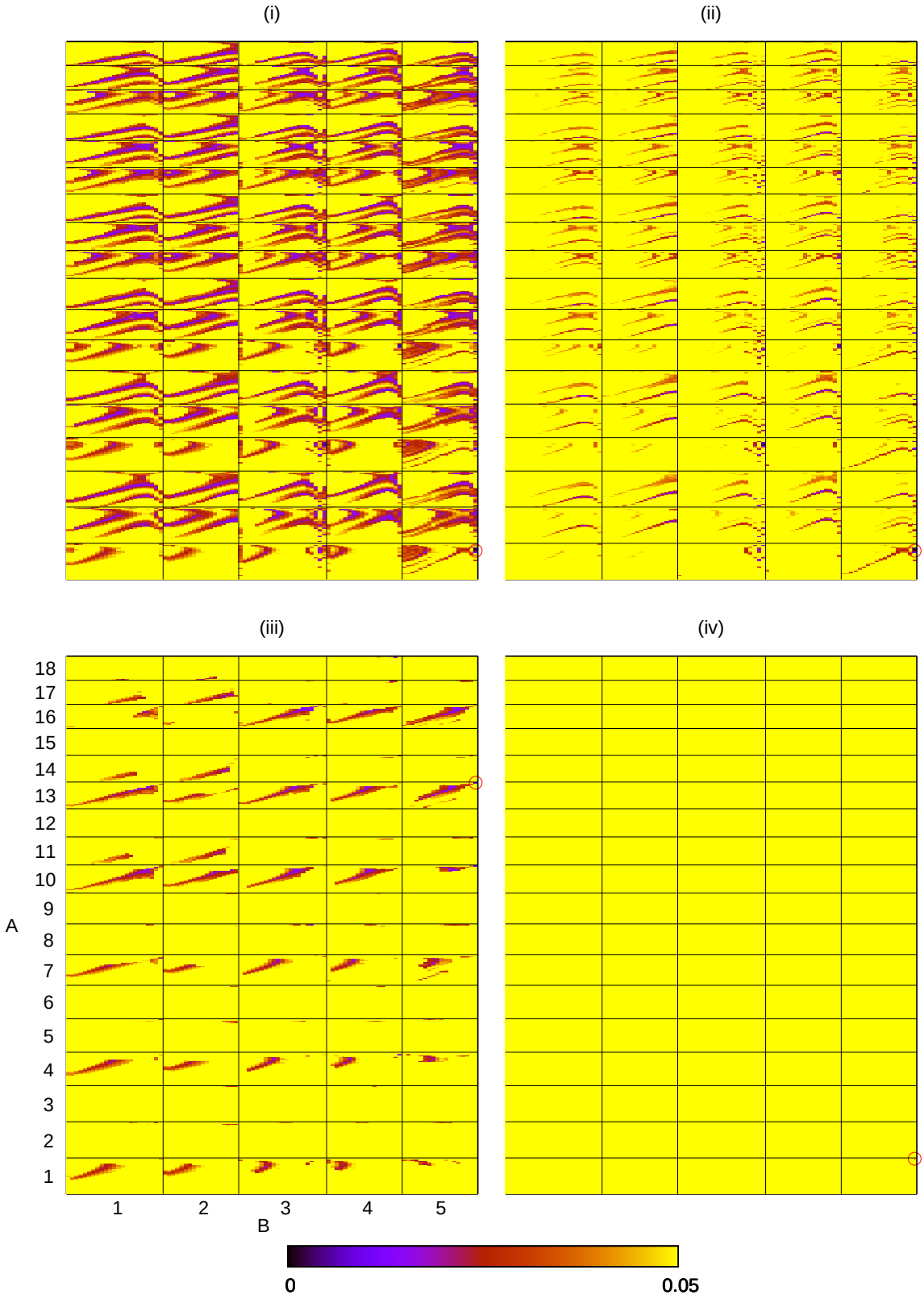

Fig. 6. Colourmap of $\mathcal{M}^2$. The models of grid *A* are plotted along the vertical axis, and the models of grid *B* along the horizontal axis. The models are divided in blocks according to evolutionary track. Where we have ordered the blocks with increasing mass (see Table 3.4), and in the blocks the models are ordered with increasing age. The four panels are for the four diferent scenarios (i), (ii), (ii) and (iv) as described in the text. In each panel with have circled the gridpoint with minimum $\mathcal{M}^2$. The frequency matching of these gridpoints can be seen in Fig. 7. Notice that panel (iv) has no significant matches, but we still circeled the one with the lowest $\mathcal{M}^2$.

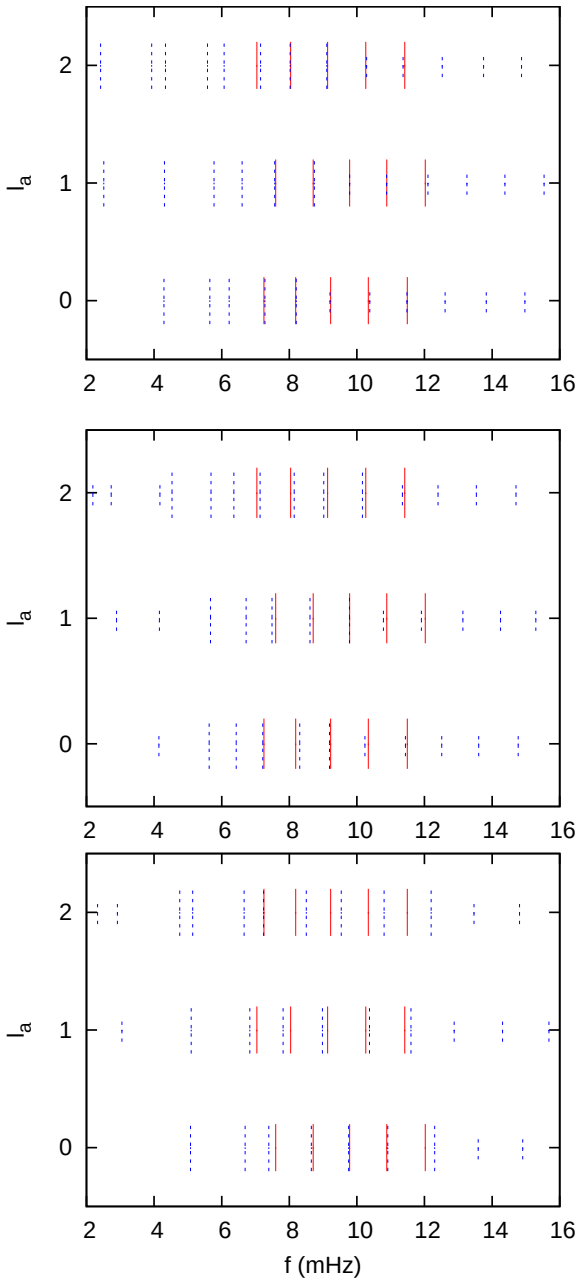

Fig. 7. The frequency matches of the minimum $\mathcal{M}^2$ gridpoints. On the vertical axis the l-value of model a is depicted. Only for (i) and (ii), this is equal to the l-value of model b. For (iii) and (iv) we have assumed that the l-value of b is not known.

compared to the total number of combinations. Furthermore, the distinction between models a and b is drastically increased if we have either mode identification or spectroscopic $\log g$ and $T_{\rm eff}$ values. From Fig. 6(iv) we see that if we only allow matching to unstable (and not stable) frequencies of a, we find no matches with $\mathcal{M}^2 < 0.05$.

4. Discussion & Conclusions

We studied the up to now neglected, post-non-degenerate sdB stars, and compared the physical and seismic characteristers with the canonical post-flash sdB stars, both formed in the CEE channel. The results presented here are a first step to observationally distinguish the two kinds of sdB stars, which is necessary

Table 2. The models with minimum $\mathcal{M}^2$ for the four different scenarios.

	(i) & (ii)	(iii)	(iv)
$\mathcal{M}^2$	0.0018	0.0082	0.080
track	*A*1	*A*13	*A*1
$M_{\rm sdB}$ ($M_\odot$)	0.42	0.46	0.42
$M_{\rm env,0}$ ($M_\odot$)	0.0001	0.0001	0.0001
$\log g$	5.69	5.69	5.78
$T_{\rm eff}(K)$	29216	33117	32187
EHB age (yr)	2.2×10^8	1.9×10^8	2.7×10^8
track	*B*5	*B*5	*B*5
$M_{\rm sdB}$ ($M_\odot$)	0.47	0.47	0.47
$M_{\rm env,0}$ ($M_\odot$)	0.005	0.005	0.005
$\log g$	5.69	5.69	5.69
$T_{\rm eff}(K)$	33558	33558	33558
EHB age (yr)	1.8×10^8	1.8×10^8	1.8×10^8

if seismic modelling is to achieve a reliable mass determination. Furthermore, the observation of a post-non-degenerate sdB star in a post-CE binary would give important constraints on the CE evolution. We plan to continue such investigations on the sdB pulsator in the post-CE, eclipsing binary PG 1336-018 which we have started in Hu et al. (2007) and Vučković et al. (2007).

Up to date, there are no evolutionary models of sdB stars available that include the coupling between diffusion and evolution consistently. This is a deficiency, since iron accumulation due to diffusion is responsible for the pulsational instability in these stars (Charpinet et al. 1996). Also, it has been shown by Fontaine et al. (2006) that the iron accumulation changes the frequencies signicantly. In our study, we have parametrized the iron accumulation due to diffusional processes, so that we can, at least in an approximative manner, take into account simultaneously the effects of diffusion and evolution on the pulsation modes.

We find that, in principle, a post-non-degenerate sdB star may appear as an EC 14026 star with similar pulsation frequencies as the canonical post-He-flash sdB star. However, additional observables, such as spectroscopic $\log g$ and $T_{\rm eff}$ determinations, and mode identification enable us to discriminate between the two different classes of sdB stars. The frequency range of the unstable modes is also an important discriminator between the two formation channels. In general, for the same $\log g$ and $T_{\rm eff}$ values, the excited frequencies of the post-non-degenerate sdB star are greater than the excited frequencies of the post-flash star. This is a direct result of the differing interior structures. Thus, special attention must be paid when observed frequencies are matched with theoretical unexcited frequencies.

We have made a modest grid of models which is sufficient for our comparative study. Detailed seismic modelling of an observed star however, will require a finer grid. For now we have chosen not to make sdB models above 0.47 $M_\odot$, since this is the maximum mass the degenerate He-core of a Red Giant with $Z = 0.02$ can have before experiencing a He-flash. A metallicity of $Z = 0.004$ allows the He-core to grow up to 0.48 $M_\odot$ on the RGB (Han et al. 2002). However, we found that in order to excite modes in these low metallicity stars, an iron enhancement greater than a factor 10 is required. This was to be expected, since Charpinet et al. (1996) found unstable pulsation modes for models with uniform $Z \geq 0.04$ in the H-rich envelope. We have therefore not pursued these models further. The question whether post-flash sdB stars can have masses > 0.47 $M_\odot$ is also

closely related to the input physics and the physics of the He-flash, and needs to be examined further.

In this paper, we have focused on the short-period *p*-mode sdB pulsators. The case of the long-periods *g*-mode sdB pulsators is, although challenging from an observational point of view, a very interesting theoretical case study. The *p*-modes probe only the most outer layers, and hence are less affected by the differing composition gradients than the *g*-modes, as they propagate deeper into the star. The long-period sdB pulstors are interpreted as cooler sdB models with much thicker hydrogen-envelopes than the short-period sdB pulsators (Fontaine et al. 2003; Jeffery & Saio 2006). Since the *g*-modes are deep interior modes, full evolutionary models including iron accumulation, as we have developed here, are required to model these stars. At present these are not available yet. We are currently developing a similar approach as presented here to study the long-period sdB models.

Acknowledgements. We are grateful to P. P. Eggleton for the use of his evolution code, and to E. Glebbeek and S. de Mink for their help with this code. We thank W. van Ham for his help with the frequency matching algorithm. We also like to thank M. Vučković, R. Østensen and M. D. Reed for stimulating discussions. HH thanks the department of Astrophysics at University of Liège, for its hospitality. HH acknowledges a PhD scholarship through the "Convenant Katholieke Universiteit Leuven, Belgium – Radboud Universiteit Nijmegen, the Netherlands". CA acknowledges financial support from the "Stichting Nijmeegs UniversiteitsFonds (SNUF)" and the Netherlands Research School for Astronomy (NOVA). HH and CA are supported by the Research Council of Leuven University, through grant GOA/2003/04. GN is supported by NWO-VENI grant 639.041.405.

References

Aerts, C., Thoul, A., Daszyńska, J., et al. 2003, Science, 300, 1926
Allard, F., Wesemael, F., Fontaine, G., Bergeron, P., & Lamontagne, R. 1994, AJ, 107, 1565
Badnell, N. R. & Seaton, M. J. 2003, Journal of Physics B Atomic Molecular Physics, 36, 4367
Brassard, P., Fontaine, G., Billères, M., et al. 2001, ApJ, 563, 1013
Canuto, V. 1970, ApJ, 159, 641
Carraro, G., Girardi, L., Bressan, A., & Chiosi, C. 1996, A&A, 305, 849
Caughlan, G. R. & Fowler, W. A. 1988, Atomic Data and Nuclear Data Tables, 40, 283
Caughlan, G. R., Fowler, W. A., Harris, M. J., & Zimmerman, B. A. 1985, Atomic Data and Nuclear Data Tables, 32, 197
Charpinet, S., Fontaine, G., Brassard, P., et al. 1997, ApJ, 483, L123+
Charpinet, S., Fontaine, G., Brassard, P., & Dorman, B. 1996, ApJ, 471, L103
Charpinet, S., Fontaine, G., Brassard, P., & Dorman, B. 2000, ApJS, 131, 223
Chayer, P., Fontaine, G., & Wesemael, F. 1995, ApJS, 99, 189
D'Cruz, N. L., Dorman, B., Rood, R. T., & O'Connell, R. W. 1996, ApJ, 466, 359
Dupret, M. A. 2001, A&A, 366, 166
Eggleton, P. P. 1971, MNRAS, 151, 351
Eggleton, P. P. 1972, MNRAS, 156, 361
Eggleton, P. P. 1973, MNRAS, 163, 279
Eggleton, P. P., Faulkner, J., & Flannery, B. P. 1973, A&A, 23, 325
Eldridge, J. J. & Tout, C. A. 2004, MNRAS, 348, 201
Fontaine, G., Brassard, P., Charpinet, S., & Chayer, P. 2006, Memorie della Societa Astronomica Italiana, 77, 49
Fontaine, G., Brassard, P., Charpinet, S., et al. 2003, ApJ, 597, 518
Green, E. M., Fontaine, G., Reed, M. D., et al. 2003, ApJ, 583, L31
Han, Z., Podsiadlowski, P., & Eggleton, P. P. 1994, MNRAS, 270, 121
Han, Z., Podsiadlowski, P., Maxted, P. F. L., & Marsh, T. R. 2003, MNRAS, 341, 669
Han, Z., Podsiadlowski, P., Maxted, P. F. L., Marsh, T. R., & Ivanova, N. 2002, MNRAS, 336, 449
Heber, U. 1986, A&A, 155, 33
Hu, H., Nelemans, G., Østensen, R., et al. 2007, A&A, 473, 569
Hubbard, W. B. & Lampe, M. 1969, ApJS, 18, 297
Iben, Jr., I. 1975, ApJ, 196, 525
Iben, Jr., I. & Renzini, A. 1983, ARA&A, 21, 271
Iglesias, C. A. & Rogers, F. J. 1996, ApJ, 464, 943
Itoh, N., Adachi, T., Nakagawa, M., Kohyama, Y., & Munakata, H. 1989, ApJ, 339, 354
Itoh, N., Mutoh, H., Hikita, A., & Kohyama, Y. 1992, ApJ, 395, 622
Jeffery, C. S. & Saio, H. 2006, MNRAS, 372, L48
Kilkenny, D., Koen, C., O'Donoghue, D., & Stobie, R. S. 1997, MNRAS, 285, 640
Ledoux, W. P. 1947, ApJ, 105, 305
Maxted, P. f. L., Heber, U., Marsh, T. R., & North, R. C. 2001, MNRAS, 326, 1391
Michaud, G., Bergeron, P., Wesemael, F., & Heber, U. 1989, ApJ, 338, 417
Miglio, A., Bourge, P.-O., Montalbán, J., & Dupret, M.-A. 2007, Communications in Asteroseismology, 150, 209
Morales-Rueda, L., Maxted, P. F. L., Marsh, T. R., Kilkenny, D., & O'Donoghue, D. 2006, Baltic Astronomy, 15, 187
Nelemans, G., Verbunt, F., Yungelson, L. R., & Portegies Zwart, S. F. 2000, A&A, 360, 1011
Pols, O. R., Schroder, K.-P., Hurley, J. R., Tout, C. A., & Eggleton, P. P. 1998, MNRAS, 298, 525
Pols, O. R., Tout, C. A., Eggleton, P. P., & Han, Z. 1995, MNRAS, 274, 964
Reimers, D. 1975, Memoires of the Societe Royale des Sciences de Liege, 8, 369
Saffer, R. A., Bergeron, P., Koester, D., & Liebert, J. 1994, ApJ, 432, 351
Schroder, K.-P., Pols, O. R., & Eggleton, P. P. 1997, MNRAS, 285, 696
Scuflaire, R., Montalbán, J., Théado, S., et al. 2007, Ap&SS, 322
Seaton, M. J. & Badnell, N. R. 2004, MNRAS, 354, 457
Seaton, M. J., Yan, Y., Mihalas, D., & Pradhan, A. K. 1994, MNRAS, 266, 805
Unglaub, K. & Bues, I. 2001, A&A, 374, 570
Vink, J. S. & Cassisi, S. 2002, A&A, 392, 553
Vučković, M., Aerts, C., Östensen, R., et al. 2007, A&A, 471, 605